A Single-Switch High-Gain PV Microconverter With Low-Switch-Voltage-to-High-Voltage-Bus Ratio

Kajanan Kanathipan, *Student Member, IEEE*, Reza Emamalipour, *Student Member, IEEE*, and John Lam, *Senior Member, IEEE*

***Abstract*—A new soft-switched, single-switch electrolytic capacitor-less step-up dc/dc microconverter for photovoltaic applications is presented in this article. The proposed circuit is an improved coupled-magnetics based single-switch topology that has low-voltage stress across the switch compared to the high voltage dc bus level (380–400 V). The proposed circuit is able to achieve zero voltage switching turn-ON and zero current switching turn-OFF for the switch. Since the input inductor in the proposed circuit operates in continuous conduction mode, the required input filter capacitance is reduced and hence, allows for the small-size nonelectrolytic capacitor to be used. The main advantage of the proposed circuit is that it is able to achieve high voltage gain while the ratio between the peak switch voltage and the output dc-bus voltage is reduced compared to other coupled-inductor based topologies. In addition, the proposed converter is able to achieve maximum power point tracking through variable switching frequency control. Results are provided on a 40-V/380-V, 200-W system to highlight the merits of the proposed circuit.**

***Index Terms*—DC-DC power converter, maximum power point tracking (MPPT), photovoltaic systems, step-up converter, zero voltage switching.**

I. Introduction

SOLAR energy has had the highest growth rate among renewable energy resources with its global capacity having increased from 6.01 to 505 GW from 2006 to 2018 [1], [2]. Solar energy is one of the more promising renewable energy resources available due to its simplicity and the advancement in solar technology. However, solar energy is unpredictable and intermittent, resulting in the lack of constant generated power at all times. The power generated from PV panels is directly affected by factors such as the position of the sun, cloud cover, temperature, and the clarity of the atmosphere. This implies the need for a method to efficiently extract power from the PV panel at various operating conditions.

As shown in Fig. 1, a typical solar panel's output voltage is much lower than the dc-bus voltage level (∼380–400 V)

Manuscript received August 26, 2019; revised December 8, 2019; accepted February 1, 2020. Date of publication February 17, 2020; date of current version May 1, 2020. This work was supported by Ontario Research Funds Program. Recommended for publication by Associate Editor M. S. ElMoursi. *(Corresponding author: Kajanan Kanathipan.)*

The authors are with the Department of Electrical Engineering and Computer Science, Lassonde School of Engineering, York University, Toronto, ON M3J 1P3, Canada (e-mail: kana0603@my.yorku.ca; remamali@cse.yorku.ca; johnlam@cse.yorku.ca).

Color versions of one or more of the figures in this article are available online at http://ieeexplore.ieee.org.

Digital Object Identifier 10.1109/TPEL.2020.2974207

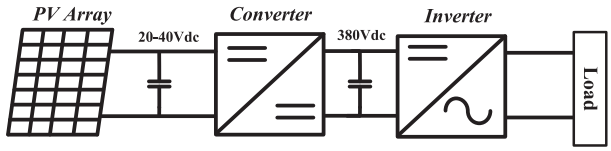

Fig. 1. Power conversion block diagram for PV systems (micro-inverter).

[3], [4] and hence, a dc/dc converter with high step-up voltage conversion ratio is required. The converter is also responsible for providing maximum power point tracking functionality. In addition, the current drawn from the PV panel must have a low ripple in order to maximize the efficiency of the MPP tracker [5]. Various step-up dc/dc converter topologies have been discussed in the literature [6]–[25] for use with solar energy systems. The basic dc/dc boost converter must operate at a high duty cycle to achieve a high voltage gain. This can result in several issues, such as a narrow turn-OFF period, high current ripple, high switch voltage, and increased switching losses [6], [7]. Alternative step-up dc/dc converter topologies have been discussed to achieve a large step-up gain [6]–[9]. For example, the converter discussed in [8] makes use of two switches and diodes to achieve a voltage gain of over two times larger than the standard boost converter. These converters also maintain a lower switch to output voltage ratio, however, they still operate with a large duty cycle. They also require multiple switches and diodes, which implies the need for the additional gate driver and heat dissipation devices. Another issue is that in most cases, these converters still require a large duty ratio to achieve high step-up voltage conversion to match the dc-bus voltage level.

One method of achieving a large step-up gain without the need for a large duty cycle is through the use of an interleaved structure [7], [10]–[13], [19]. Interleaved structures also bring the benefit of low-input current ripple and small magnetic components. However, one drawback is the increased converter size due to multiple semiconductor components. For example, the circuit presented in [7] makes use of two interleaved boost converters and a voltage multiplier cell to achieve a gain of around ten with a duty cycle close to 70%. In the case of the interleaved structure discussed in [10] and [19], several of its semiconductor switches are not connected to ground, which implies the need for additional isolation devices.

In order to circumvent these issues, coupled inductor based dc/dc step-up converters that do not require the use of large duty ratio have been reported [14]–[18], [20], [21], [23]. For

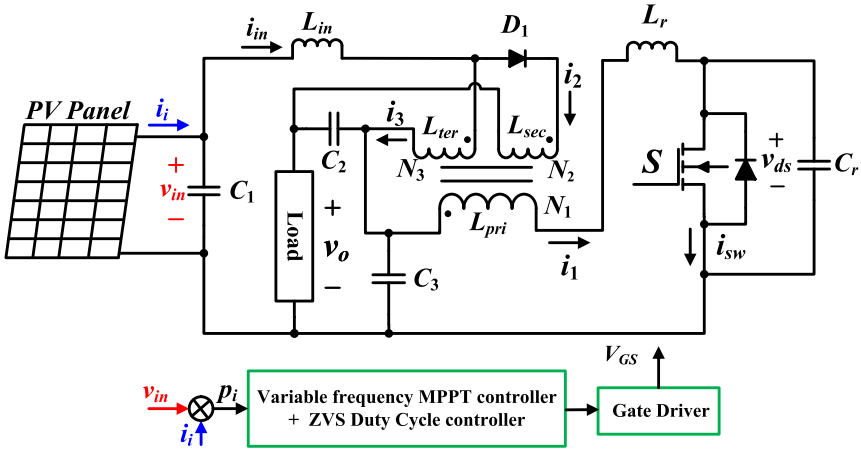

Fig. 2. Proposed single-switch dc/dc step-up converter for PV application.

instance, the circuits discussed in [14] and [15] achieve a large step-up ratio while utilizing a medium duty cycle. In both cases, the converters require multiple switches, with some of them operate under hard switching [14]. Single-switch coupled inductor topologies operating without soft-switching, leading to larger component sizes due to their low-switching frequency are discussed in [20] and [23]. Single-switch coupled inductor based dc/dc converter topologies with soft-switching operating have been presented in [17] and [18]. However, the switch in both circuits suffers from a very high voltage stress. In [17], it was reported that the switch voltage to output voltage ratio is greater than 1, while in [18], the ratio is greater than 2 in all operating conditions. This implies the converter operates with a peak switch voltage of close to 800 V, which is not very practical.

Several aforementioned step-up PV microconverters [5], [17] do not require any electrolytic capacitors in their circuits. It is known that electrolytic capacitors have an energy density greater than that of film and ceramic capacitors at the same rated voltage. However, the lifetime expectancy of an electrolytic capacitor is much less than that of the overall converter and they are prone to large failure rates according to [26] and [27]. Through input current ripple minimization, these capacitors can be replaced with small-sized nonelectrolytic capacitors to improve the lifetime expectancy.

In this article, a soft-switched electrolytic capacitor-less single-switch step-up converter for photovoltaic energy application is presented. The proposed converter is an improved coupled inductor based topology that has a low ratio of switch voltage to the high voltage dc bus value. Hence, compared to other reference coupled inductor based topologies, the proposed converter has much lower voltage stress across the switch. Quasi-resonant zero-voltage switching condition is employed with the single-switch to improve the overall efficiency by minimizing the switch power loss. By operating the input inductor of the converter in continuous conduction mode with a low current ripple, a small-sized nonelectrolytic capacitor can be employed at the input, removing the need for an electrolytic-capacitor. Through the use of variable frequency control, the converter can operate at the solar input's maximum power point, allowing for efficient extraction of solar energy.

This article is organized as follows. Section II provides a description and the operating principles of the proposed step-up microconverter. Section III provides the theoretical analysis and design equations of the proposed circuit. Section IV provides the simulation and experiment results on a 40-V/380-V, 200-W prototype to highlight the merits of this work. Finally, concluding remarks and discussions are provided in Section V.

II. Circuit Description and Operating Principles

The proposed quasi-resonant single-switch step-up coupled-inductor circuit is shown in Fig. 2. The quasi-resonant zero-voltage switching (ZVS) condition is achieved through the use resonant inductor (L_r) and resonant capacitor (C_r). The switch is controlled through the use of variable switching frequency and duty cycle. Variable switching frequency control is employed when operating in maximum power point tracking mode such that the maximal amount of energy can be extracted from the PV panel. Operating at a different frequency can affect the converters' soft-switching operation. As a result, variable duty cycle control is also employed to maintain a larger frequency range for soft-switching. The circuit contains a three-winding coupled inductor with an inverted polarity for the primary winding. The secondary winding has one node connected to the load while the other is connected to a diode D_1. The tertiary winding is connected between the input inductor and the two output capacitors. The secondary winding allows for the converter to achieve a high-gain while the tertiary winding allows the converter to achieve both CCM operation and a low switch voltage. For this coupled inductor, the positive node of the primary winding is directly connected to the negative of the tertiary winding. The three winding coupled inductor follows the same principle as a transformer as it can be modeled as a transformer with the magnetizing inductance representing the primary winding. The secondary and tertiary winding inductance can then be determined through the turns ratio (1) where N_x is the turns

for winding x. There is a mutual inductance between each of the three windings as shown in (2). From here, the voltage across each winding can be determined (3)–(5)

$$L_p = L_s\left(\frac{N_1}{N_2}\right)^2 = L_t\left(\frac{N_1}{N_3}\right)^2 \tag{1}$$

$$M_{12} = \frac{L_p N_1 N_2}{{N_1}^2} M_{13} = \frac{L_p N_1 N_3}{{N_1}^2} M_{23} = \frac{L_p N_2 N_3}{{N_1}^2} \tag{2}$$

$$v_{\text{pri}} = L_p\frac{di_1}{dt} - M_{12}\frac{di_2}{dt} - M_{13}\frac{di_3}{dt} \tag{3}$$

$$v_{\text{sec}} = L_s\frac{di_2}{dt} - M_{12}\frac{di_1}{dt} + M_{23}\frac{di_3}{dt} \tag{4}$$

$$v_{\text{ter}} = L_t\frac{di_3}{dt} - M_{13}\frac{di_1}{dt} + M_{23}\frac{di_2}{dt}. \tag{5}$$

From (3)–(5), it can be seen that the primary winding voltage is related to the current flowing through the resonant inductor (i_1) as well as the current flowing through the input inductor (i_2 and i_3). It can also be understood that during the stages when the secondary winding diode is inactive there is no current flowing through the secondary winding and as a result, this current does not contribute to (3)–(5). The proposed converter consists of two output capacitors labeled C_2 and C_3 as seen in Fig. 2. The voltage across each capacitor can be determined by applying Kirchhoff's voltage law to the loop containing the input capacitor C_1, input inductor L_{in}, tertiary winding L_{ter}, and the output capacitor C_3

$$v_{c_1} = -v_{\text{Lin}} + v_{\text{ter}} + v_{c_3}. \tag{6}$$

From the voltage-second balance principle, it is understood that the average voltage across an inductor is zero. By applying this principle to (6), it can be seen that the voltage across the capacitor C_3 is equal to the input voltage throughout all operating stages and as a result, the voltage across the capacitor C_2 is the difference between the input and output voltages as follows:

$$v_{c_2} = v_o - v_{c_3}. \tag{7}$$

The theoretical operating waveforms of the proposed converter are shown in Fig. 3. These waveforms are broken down into five operating stages whose time duration ranges from t_0 to t_5. Fig. 4(a)–(e) shows the equivalent circuit during each operating stage.

Stage I [$t_0 < t < t_1$]: At time t_0, switch S is turned OFF and the current (i_1) that was flowing through S is redirected to the resonant capacitor. Due to positive i_1, the resonant capacitor begins to charge. By applying KVL to resonant capacitor (C_r), resonant inductor (L_r), primary winding (L_p), and the output capacitor (C_3) as shown in (8), it can be seen that in order for the resonant capacitor to being to charge the voltage across the resonant inductor and primary winding must decrease. This implies that i_1 is decreasing. Based on the coupled-inductor voltage relationship, it can be understood that the secondary winding voltage also decreases. This results in a decrease in the voltage across the secondary winding diode. The effective resonant frequency and the characteristic impedance of this stage

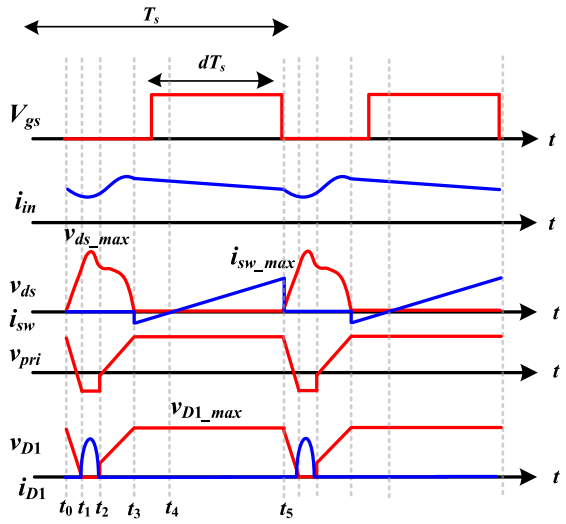

Fig. 3. Theoretical operating waveforms of the proposed converter.

are a function of the L_r, L_p, L_{in}, and the ratio between the tertiary and primary winding, as shown in (9) and (10) respectively. This stage ends at t_1 when the diode voltage (v_{D1}) reaches zero, where t_1 is given in (11), with A, B, and C given in (12)–(14), respectively

$$v_{c_3} = v_{\text{pri}} + v_{Lr} + v_{c_r} \tag{8}$$

$$\omega_0 = \frac{1}{\sqrt{\frac{L_p L_{\text{in}} + L_{\text{in}} L_r + L_r L_p n_3^2}{L_{\text{in}} + L_p n_3^2} C_r}} \tag{9}$$

$$Z = \sqrt{\frac{\frac{L_p L_{\text{in}} + L_{\text{in}} L_r + L_r L_p n_3^2}{L_{in} + L_p n_3^2}}{C_r}} \tag{10}$$

$$t_1 = \frac{1}{\omega_0}\left(\sin^{-1}\left[\frac{C-B}{\sqrt{A^2+B^2}}\right] - \cos^{-1}\left[\frac{A}{\sqrt{A^2+B^2}}\right]\right) \tag{11}$$

$$A = i_{Lr}(t_0)\, Z \tag{12}$$

$$B = v_i \tag{13}$$

$$C = \left[1 + \frac{L_{\text{in}} + L_p N_3^2}{L_p L_{\text{in}}}\right]\left[v_i - \frac{v_o - v_i}{n_2 - n_3}\right]. \tag{14}$$

Stage II [$t_1 < t < t_2$]: At time t_1, current flows through the secondary winding diode and the circuit enters a second resonant stage. In this stage, the resonant inductor and capacitor begin to resonate and exchange energy. Only L_r and C_r contribute to the effective resonant inductance given in (15) and characteristic impedance given in (16) for the duration of this stage. This results in a sinusoidal waveform for the resonant capacitor voltage and current as given in (17) and (18), respectively

$$\omega_0 = \frac{1}{\sqrt{L_r C_r}} \tag{15}$$

$$Z = \sqrt{\frac{L_r}{C_r}} \tag{16}$$

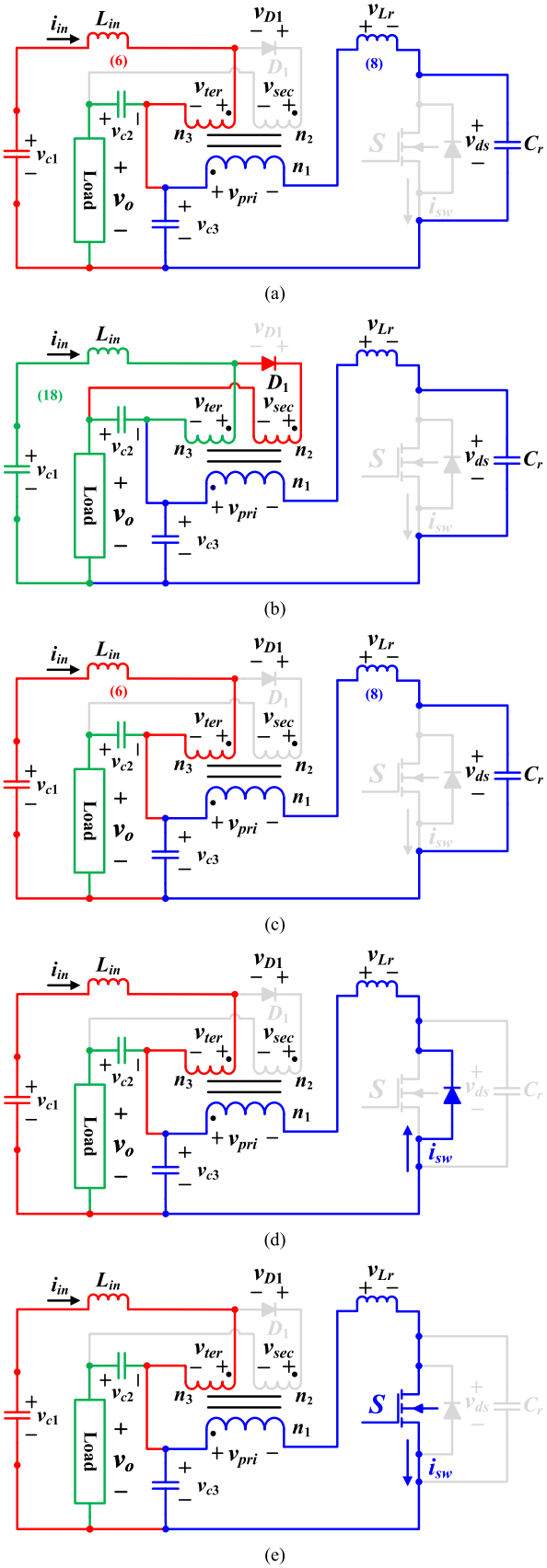

Fig. 4. Equivalent circuit during each operating stage. (a) Stage I: $[t_0, t_1]$. (b) Stage II: $[t_1, t_2]$. (c) Stage III: $[t_2, t_3]$. (d) Stage IV: $[t_3, t_4]$. (e) Stage V: $[t_4, t_5]$.

$$v_{ds} = v_i - v_{\text{pri}} + i_{lr}(t_1)\, Z \sin(\omega_0 t) - (v_i - v_{\text{pri}} + v_{ds}(t_1)) \cos(\omega_0 t) \tag{17}$$

$$i_{Lr} = \frac{(v_i - v_{\text{pri}} - v_{ds}(t_1))}{Z} \sin(\omega_0 t) + i_{Lr}(t_1) \cos(\omega_0 t). \tag{18}$$

Unlike the previous stage, the voltage across each of the coupled inductor windings is constant. Through substitution of (6) into (19), the voltage across the primary winding can be determined (20) and can be seen to be a function of the input voltage, output voltage, and the turns ratio of the secondary and tertiary winding

$$v_{c_1} = -v_{\text{Lin}} + v_o + v_{c2} \tag{19}$$

$$v_{\text{pri}} = \frac{v_o - v_i}{n_3 - n_2}. \tag{20}$$

The resonant inductor's current continues to decrease while the resonant capacitor voltage charges until it reaches its maximum value as given in (20)

$$v_{ds_{\max}} = v_i - v_{\text{pri}} + i_{Lr(t_0)} Z. \tag{21}$$

During this stage diode D_1 is ON, i_{D1} is then given in (22) and it is comprising both linear and sinusoidal components, where D and E are given in (23) and (24), respectively. Stage II ends when i_{D1} reaches zero

$$i_{D1} = D\,[t - \sin(\omega_0 t)] - E\,[\cos(\omega_0 t) - 1] \tag{22}$$

$$D = \frac{v_{\text{pri}}}{\omega_0 (n_2 - n_3)} \left[\frac{L_{\text{in}} + L_p n_3^2}{L_{\text{in}} L_p}\right] \tag{23}$$

$$E = \frac{i_{lr}(t_1)}{n_2 - n_3}. \tag{24}$$

Stage III $[t_2 < t < t_3]$: The secondary winding diode D_1 is now OFF, which results in the disconnection of the secondary winding from the circuit. The converter has the same operating components as stage I; however, the initial conditions for the circuit parameters are different. The resonant inductor current is positive and decreasing. As a result, the resonant capacitor begins to charge until the inductor current reaches zero. At this point, the resonant capacitor voltage reaches a second peak. The capacitor now begins to discharge until its voltage reaches zero. This stage ends at t_3, which is given in (25), where F, G, and H are provided in (26)–(28), respectively

$$t_3 = \frac{1}{\omega_0}\left[\cos^{-1}\left(\frac{H}{\sqrt{F^2 - G^2}}\right) + \tan^{-1}\left(\frac{G}{F}\right)\right] \tag{25}$$

$$F = -i_{lr}(t_2) \times Z \tag{26}$$

$$G = v_{sw}(t_2) - v_i \tag{27}$$

$$H = -v_i. \tag{28}$$

Stage IV $[t_3 < t < t_4]$: The resonant inductor current flowing through the resonant capacitor is now redirected to the switch. As this current is negative, it flows through the switch's antiparallel diode [see Fig. 4(d)]. By applying the gate signal to the switch

before the current becomes positive the switch will transition to the on state under ZVS operation.

Stage V [$t_4 < t < t_5$]: The gate signal is applied to the switch which turns ON at zero current. Once the current has become positive, it begins to flow through the switch while continuing to increase as the voltage across the resonant inductor is positive [see Fig. 4(e)]. The switch current increases at a rate given in (29). Once the gate signal is removed from the switch, the circuit rerenters the first stage. During this stage, the current flowing through the input inductor is decreasing at a rate given in (30). For both (29) and (30), it can be seen that the rate of change is linear. This implies the voltage across each coupled inductor winding and the secondary winding diode is constant. The voltage across the diode during stage V is provided in (31). By comparing (20) and (31), it can be understood that (31) can be obtained by solving for v_{pri} when the diode voltage is zero

$$\frac{di_1}{dt} = v_i \left[\frac{L_{\text{in}} + L_p n_3^2}{L_p L_r n_3^2 + L_{\text{in}} L_p + L_{\text{in}} L_r} \right] \tag{29}$$

$$\frac{di_3}{dt} = v_i \left[\frac{L_p n_3}{L_p L_r {n_3}^2 + L_{\text{in}} L_p + L_{\text{in}} L_r} \right] \tag{30}$$

$$v_{D1} = v_o - v_i - v_{\text{pri}} \left(n_3 - n_2 \right). \tag{31}$$

III. Design Equations of the Proposed Circuit

A. Voltage Gain Expression

The voltage gain of the proposed converter can be obtained by applying the volt-second balance principle to the primary winding. The total time duration of each stage as well as the voltage across the primary winding has been determined in terms of known parameters. As the average primary winding voltage is zero, the gain can be isolated. Equation (32) shows the voltage gain of the proposed converter where $t_1 - t_5$ represents the time duration of stages I–V, respectively, and L_α represents a combination of various inductances in the converter (33). It can be seen from (32) that the converter operates as a step-up converter as its minimum gain is 1

$$\frac{v_o}{v_i} = 1 + (n_2 - n_3) \frac{\left(\frac{t_3}{2} + \frac{1}{L\alpha} \left(t_4 + t_5 + \frac{t_1}{2} + \frac{t_3}{2} \right) \right)}{t_2 + \frac{t_1}{2}} \tag{32}$$

$$L_\alpha = \frac{L_p L_r n_3^2 + L_{\text{in}} L_p + L_{\text{in}} L_r}{L_{\text{in}} L_p}. \tag{33}$$

The operating frequency of the proposed converter has an impact on the time duration of each mode of operation. As a result, the operating frequency also affects the gain of the converter. Fig. 5 shows the gain of the converter as a function of the operating frequency. Here, it can be seen that the gain of the converter is inversely proportional to the switching frequency. As the frequency increases the gain of the converter approaches one. This matches with the expected operation of quasi-resonant zero voltage switching converters.

B. Voltage Stress

The peak switch voltage occurs during the operating cycle of stage II where the sinusoidal switch voltage increases until the current through the resonant capacitor reaches zero. Unlike the switch, the peak diode voltage stress occurs during the operating stage V and is constant throughout the stage. Both voltages are a function of the output voltage and as a result, vary with the operating frequency. Fig. 6 shows the peak switch and diode voltage to output voltage ratio at various operating frequencies. In the case of the switch voltage, there is an operating frequency at which the minimum ratio is obtained. For the diode the ratio increases as the operating frequency increases. However, it should be noted that as this is a quasi-resonant converter, the gain decreases as the frequency increases. This implies that although the ratio is higher at larger frequencies the peak diode voltage at this point may be lower than when operating at a lower frequency. As a result, the diode rating should be chosen based on the operating frequency and the expected output voltage of the converter. The voltage ratio between the switch and the output also varies based on the loading condition. Fig. 7 shows this ratio as a function of the operating frequency at different loading conditions. It can be understood at that lower loading conditions the ratio between the switch and the output voltage is lower. The required operating frequency to obtain the minimum ratio is also proportional to the loading.

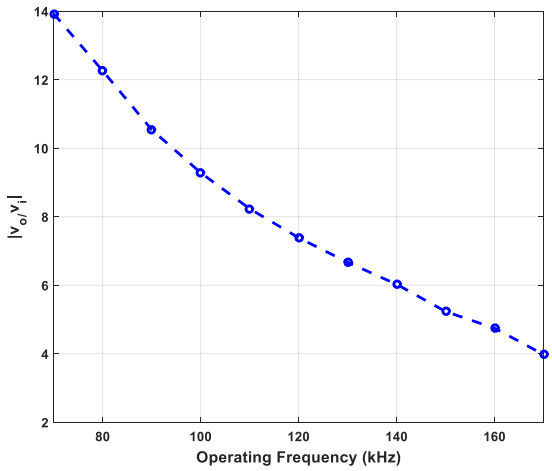

Fig. 5. Gain as a function of frequency for the proposed converter.

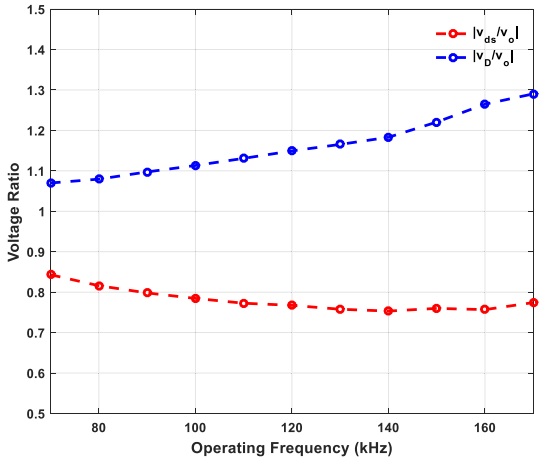

Fig. 6. Voltage ratio for the proposed converter.

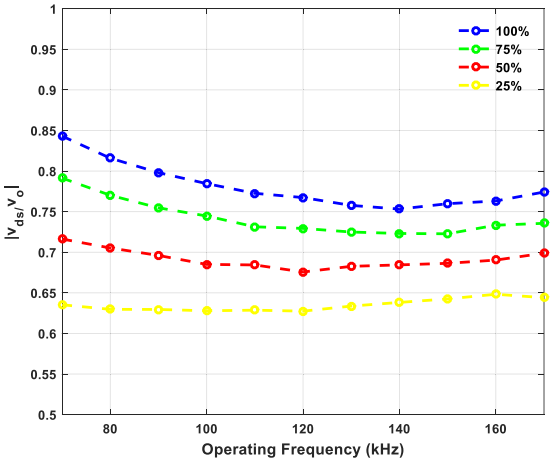

Fig. 7. Switch to output voltage ratio at different loading conditions.

C. Duty Cycle

As previously mentioned, varying the operating frequency of the converters switch affects soft-switching operation. In order to overcome this issue, the duty cycle of the converter's switch can be varied. The switch voltage is greater than zero during stages I–III as shown in Fig. 3. This implies that the gate signal must be applied to the switch after stage III but before the switch current becomes positive. As a result, the minimum duty cycle required for soft-switching operation is (33)

$$D_{\min} = \frac{t_1 + t_2 + t_3}{T}. \tag{34}$$

The maximum duty cycle at which the circuit can operate under soft-switching condition is the time taken until the switch current becomes positive. This can be solved for by applying (28) to determine the time period taken for the current to become positive after the converter has entered stage IV (34)

$$D_{\max} = D_{\min} + \frac{i_{Lr(t_3)}}{v_i \left[\frac{L_{in}+L_p {n_3}^2}{L_p L_r n_3^2 + L_{\text{in}} L_p + L_{\text{in}} L_r}\right]}. \tag{35}$$

D. Coupled Inductor

The proposed converter consists of a three-winding coupled inductor. Design requirements on the windings exist as the ratio between the windings affect the converter gain, switch voltage, switch current, and soft-switching operation. The ratio between the tertiary and primary winding has a large impact on the peak switch current. During stage IV the switch current is increasing linearly as a function of the tertiary winding. This implies that a larger ratio between the tertiary and primary winding results in a larger peak switch current. If the ratio between the three windings are 1:1:1 or 1:x:x the gain of the converter will be 1 as seen in (32). It can also be understood that to achieve a large step-up gain the ratio between the secondary and tertiary winding must be significant, however, operating at a large ratio has an impact on soft-switching. The resonant inductor current is affected by this ratio, with a larger ratio resulting in a steeper increase in this current. This can result in a positive current before the resonant capacitor has fully discharged, resulting in hard-switching operation. The peak switch voltage is provided in (21) and is seen to be a function of the coupled inductor winding (through v_{pri}) and the resonant inductor current at the start of stage I. This is the same value as the peak switch current, which was previously mentioned to be a function of the tertiary winding. This implies the ratio between the tertiary winding and the primary winding has a larger impact on the peak switch voltage compared to the secondary winding.

E. Resonant Parameters

As with the previously discussed parameters and components, the resonant capacitor and inductor have an impact on the circuit operation. As the proposed converter is a quasi-resonant based converter its gain is affected by ratio between the operating frequency and the resonant frequency. When this ratio increases the gain of the converter decreases as seen in Fig. 5. This causes restrictions on the resonant capacitor and inductor values. From (17) and (18), it can be seen that both the peak switch current and voltage are affected by the resonant inductor parameter. The switch voltage is also affected by the characteristic impedance Z which in turn is a function of the resonant parameters.

F. RC Snubber Circuit

The converter's coupled inductor has a leakage inductance that resonates with the output capacitance of the diode during operation. This results in oscillations in the diode voltage and switch current waveform. In order to mitigate this, an RC snubber circuit was employed in parallel with the secondary winding diode. The capacitance (36) and resistance (37) for the snubber were determined based on the ringing frequency and leakage inductance

$$c_p = \frac{1}{(2\pi f_r)^2 L_p} \tag{36}$$

$$R_s = Z_p = \sqrt{\frac{L_p}{c_p}} \tag{37}$$

$$P_L = c_p {v_D}^2 f. \tag{38}$$

The addition of the snubber circuit introduces additional losses into the system. The power loss associated with this circuit is provided in (38) where V_D is the diode voltage and f is the operating frequency.

G. Maximum Power Point Tracking Controller

During operation with a solar panel, the converter's operating frequency was varied through an MPPT controller. The controller is based on a modified frequency based perturb and observe method discussed in [28] with an additional check to minimize oscillation around the MPP. The operating voltage and current are obtained through sensors and various comparisons are performed to determine which direction the frequency should be changed to achieve MPP operation. The additional oscillation minimization check also reduces the variation in the peak switch voltage and current. Fig. 8 shows a flowchart depicting the controller function.

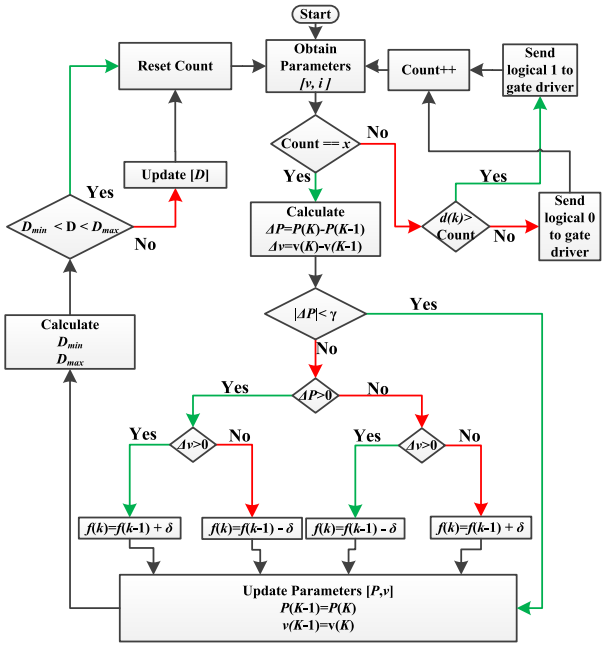

Fig. 8. MPPT flowchart.

TABLE I
CONVERTER DESIGN SPECIFICATIONS AND PARAMETERS

CONVERTER DESIGN SPECIFICATIONS	
Output Voltage (v_o)	380V
Input Voltage (v_{in})	40V
Operating Frequency (f)	80kHz – 150kHz
CONVERTER CIRCUIT PARAMETERS/PART NUMBER	
Input Capacitor (C_1)	20 µF
Output Capacitor (C_2)	50 µF
Output Capacitor (C_3)	20 µF
Resonant Capacitor (C_r)	36 nF
Input Inductor (L_{in})	270 µH
Resonant Inductor (L_r)	1.5 µH
Magnetizing Inductance of Transformer (L_p)	18 µH
Turns Ratio (n_1: n_2: n_3)	2:8:3
Switch (S)	FDPF2710T (250V, 25A)
Diode (D_1)	MURS360BT3G (600V, 3A)

IV. Simulation and Experimental Results

A. Simulation Results

To verify the performance of the proposed topology, simulation results are first obtained on a 100 kHz, with an input voltage of 40 V with an output power of 200 W system. Table I shows the system parameters. The resonant components were chosen based (17) and (18) to obtain a low peak switch voltage. The primary and tertiary winding ratio was chosen based on the desired voltage stress. The secondary and tertiary winding ratio was chosen to achieve the required gain based on the chosen components. Fig. 9(a) shows the output voltage (v_o) and switch voltage (v_{ds}) when operating with an input voltage of 40 V and

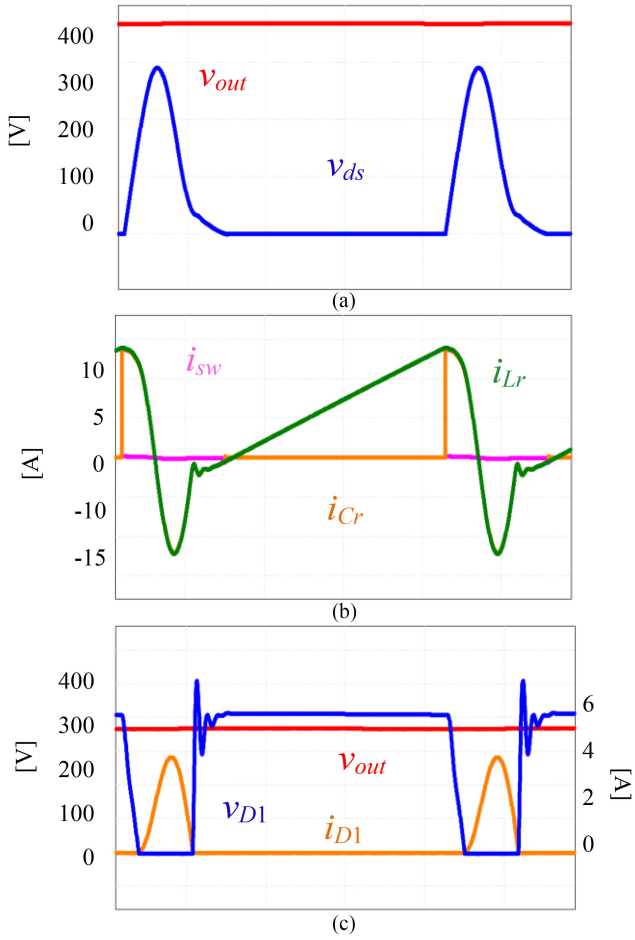

Fig. 9. Simulation results. (a) Switch and output voltage. (b) Switch, resonant capacitor, and resonant inductor current. (c) Diode voltage and current.

at a frequency of 100 kHz. The peak switch voltage is much lower than the output voltage with a ratio of 0.78:1. Fig. 9(b) shows the switch, resonant inductor, and resonant capacitor current waveform. It can be seen that the circuit operates under the soft-switching condition. At the point, the switch current drops to zero the circuit transitions to stage I and the current is redirected to the resonant capacitor. The diode voltage, current, and output voltage waveforms are shown in Fig. 9(c), which shows that the diode operates under soft-switching operation. The overall system efficiency was 94%. The MPPT performance was then examined with a solar panel at the input. The light intensity was varied from 200 to 700 W/m^2. Fig. 10(a) shows the MPPT performance of the proposed circuit. The switch voltage and current are shown in Fig. 10(b) and (c), respectively, and can be observed to operate under soft-switching conditions at all switching frequencies. The ratio between the peak switch voltage and the output voltage was less than 0.8 throughout the circuit operation.

B. Hardware Prototype

A proof-of-concept 200-W hardware prototype was constructed. Fig. 11 shows the picture of the prototype. The three winding coupled inductor has a turns ratio of 2:8:3 with a

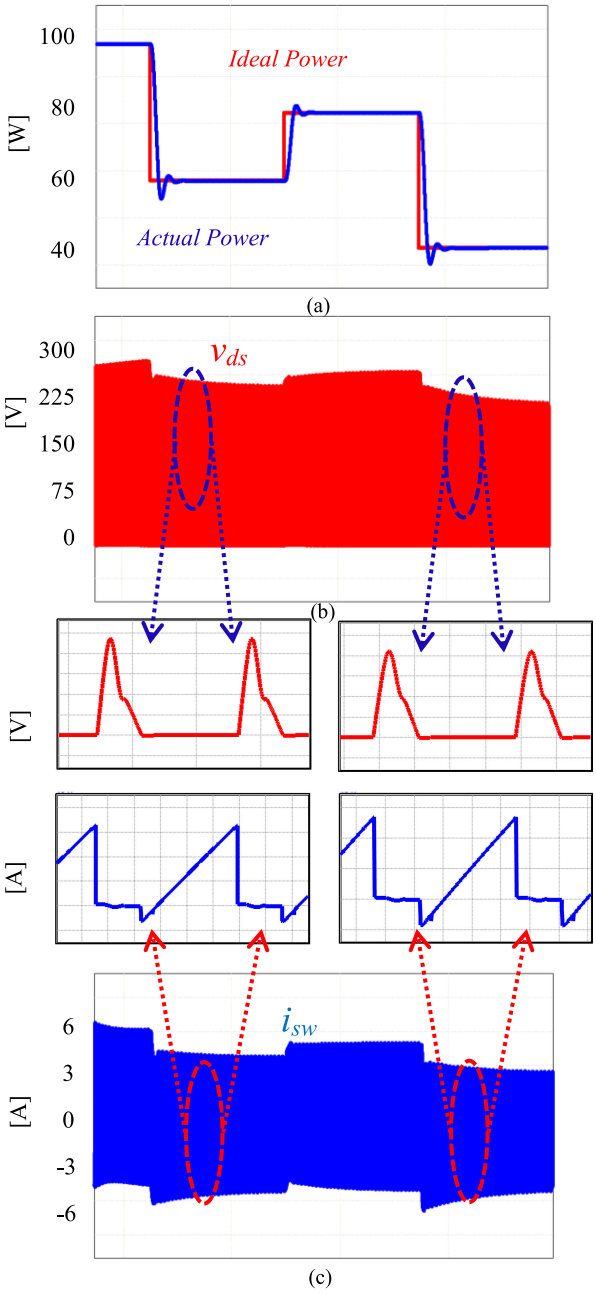

Fig. 10: Simulation results. (a) Light intensity. (b) Theoretical power and obtained input power. (c) Switch voltage. (d) Switch current.

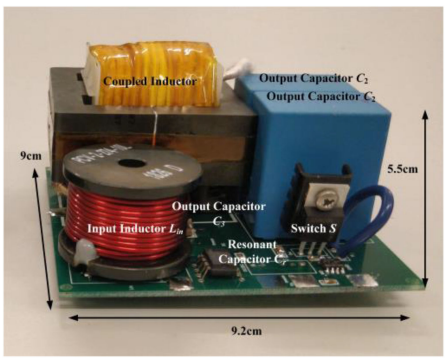

Fig. 11. Hardware prototype.

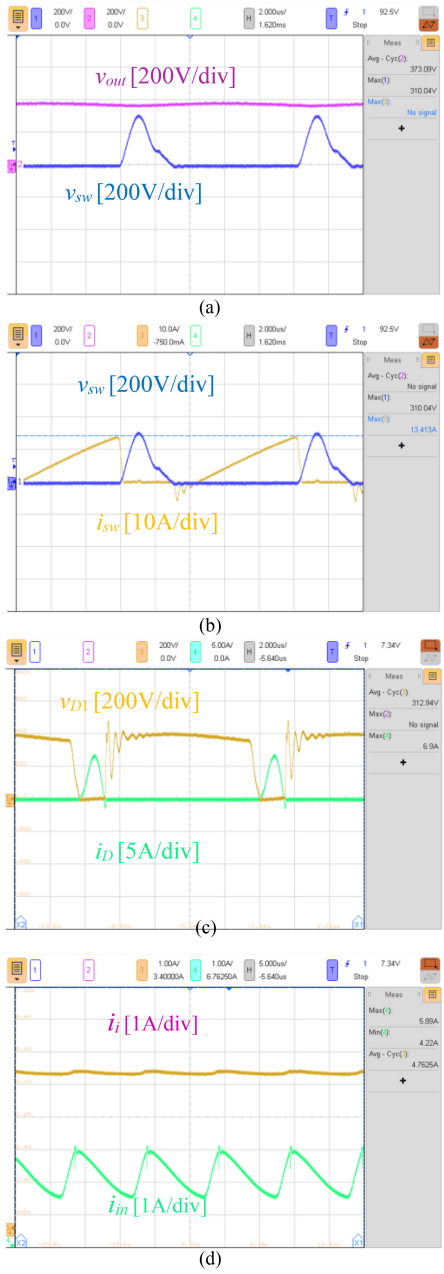

Fig. 12. Hardware waveforms. (a) Switch and output voltage. (b) Switch voltage and current. (c) Diode voltage and current. (d) Input and input inductor current.

magnetizing inductance of 18 μH. The resonant components were chosen to be 1.5 μH and 36 nF, respectively, to achieve a switching frequency to output frequency ratio of 0.1 when operating at 100 kHz. Fig. 12(a) shows the switch voltage and output voltage. The peak switch voltage was measured to be 310 V while the output voltage was around 373 V. This results in a switch voltage to an output voltage ratio of 0.83:1. The prototype converter was found to operate under soft-switching conditions as the switch current is positive well after the resonant capacitor has discharged. This can be observed in Fig. 12(b), which shows the switch current and voltage waveforms. The diode voltage and current waveforms are shown in Fig 12(c).

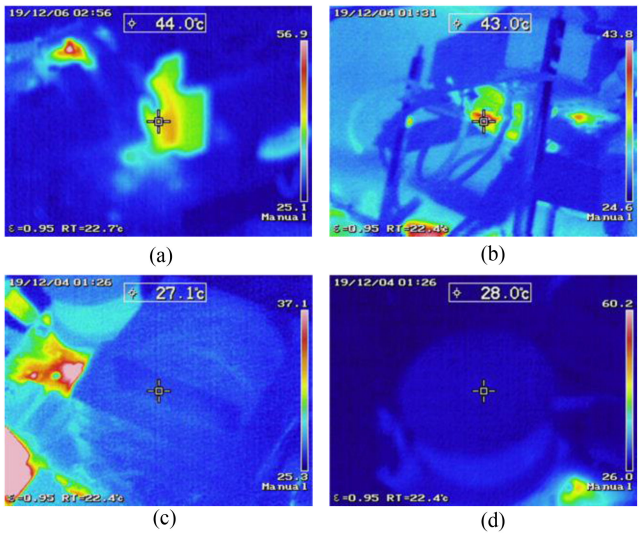

Fig. 13. Hardware thermal measurements. (a) Switch. (b) Diode. (c) Coupled inductor. (d) Input inductor.

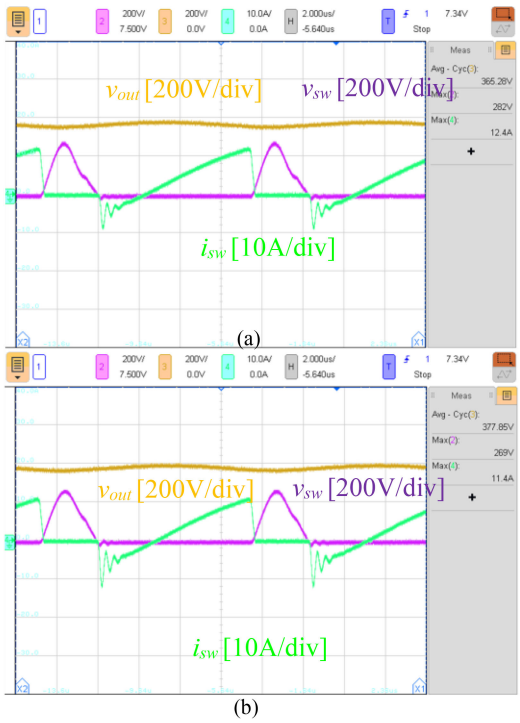

Fig. 14. Converter's switch and output waveforms at (a) 58% loading and (b) 35% loading.

The steady-state diode voltage is approximately 400 V which is in agreement with (30). The converters diode is seen to operate under soft-switching condition as the diode voltage is zero before the current begins to flow through it. The input current and input inductor current are shown in Fig. 12(d) with a very low input current ripple. The efficiency of the hardware prototype was 94%. Fig. 13 shows the thermal images of the proposed system. The switch is shown to be operating at a temperature of 44.0 °C in Fig. 13(a). During steady-state operation, the diode temperature was 43.0 °C. The steady-state temperature of the input inductor

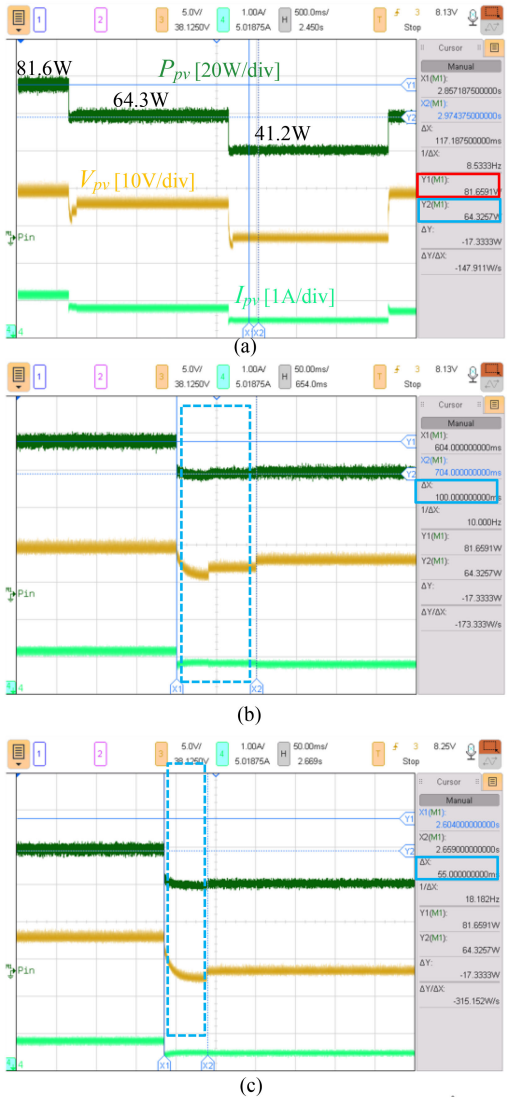

Fig. 15. (a) Experimental results for 300–600 W/m^2. (b) 100 ms to reach MPP. (c) 55 ms to reach MPP.

and the three-winding coupled inductor are shown in Fig. 13(c) and (d) respectively. Fig. 14 shows the proposed converter operating at loading conditions of 58% and 35%, respectively. The converter is still able to achieve soft-switching operation while maintain a low switch to output voltage ratio. The efficiency was 93% and 92%, respectively. The MPPT performance of the hardware prototype was verified through a Keysight E4360A Solar Array Simulator. A TMS320F28335 DSP board was used as the MPPT controller. The operating light intensity was varied between 300 W/m^2 and 600 W/m^2 every two seconds. Fig. 15(a) shows the panel power, voltage, and current waveforms during operation with the MPPT controller. By comparing the obtained panel power to the maximum power provided by the panel software in Fig. 16, it can be understood that the controller successfully brought the converter to the maximum power point of the input panel. From Fig. 15(b) and (c), it can be observed that the MPPT controller is able to track the MPP in 100 ms or less.

TABLE II
COMPARISON WITH OTHER STEP-UP DC/DC CONVERTERS

CONVERTER	NUMBER OF COMPONENTS				PEAK SWITCH VOLTAGE	GAIN	COUPLED INDUCTOR	SWITCHING TYPE	OPERATING FREQUENCY	MAXIMUM POWER LEVEL	EFFICIENCY
	S	D	C	L							
[13]	1	4	5	2	$\frac{v_i}{1-D}$	11	Yes	Hard	30kHz	220W	94%
[19]	2	3	5	1	$\frac{v_o}{(1+n(2-D))}$	7-9.5	Yes	Soft	60kHz	250W	95%
[20]	1	3	4	2	$\frac{v_o}{N+2}$	10	Yes	Hard	30kHz	225W	93%
[21]	1	2	1	3	$\frac{v_i}{1-D}$	20	Yes	Hard	24kHz	100W	92%
[22]	2	2	3	2	v_{Co1}	9.5	No	Soft	70kHz	250W	90.5%
Proposed Converter	1	1	4	3	$v_i - v_{pri} + i_{Lr(t_0)}Z$	9.5	Yes	Soft	80-150kHz	200W	94%

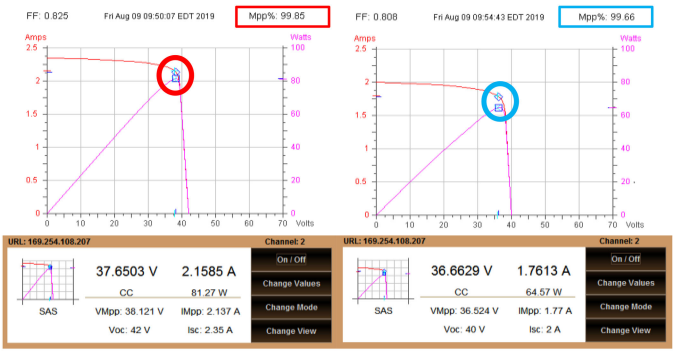

(a) (b)

Fig. 16. Operating condition of the solar emulator. (a) 81.27 W. (b) 64.57 W.

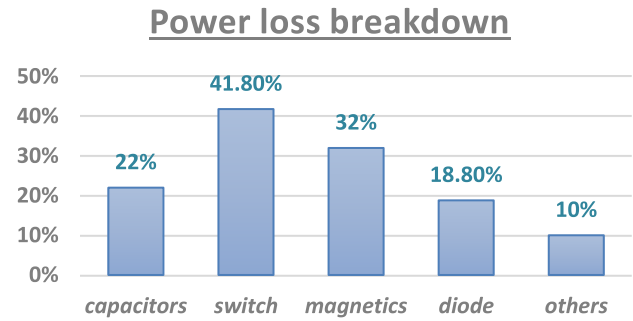

Fig. 17. Power loss breakdown of the proposed converter at rated power.

Table II provides the comparison of the proposed converter with other dc/dc converters designed for renewable energy systems. The proposed converter has the lowest component count out of all types of converters. When compared to other single-switch soft-switching coupled-inductor based topologies, the proposed converter is able to obtain the same circuit gain while minimizing the ratio between the peak switch voltage and the output voltage.

Fig. 17 shows the power loss breakdown for the proposed converter when operating at the rated power. The switch conduction losses were found to contribute the most to the efficiency loss. This can be improved by utilizing a switch with a lower drain-to-source resistance.

V. CONCLUSION

A soft-switched, single-switch coupled-inductor based dc/dc converter for photovoltaic energy application has been presented. The converter is able to achieve a high step-up voltage gain while minimizing the ratio between the switch voltage and the output voltage. The proposed converter achieves soft-switching operation at all conditions. MPPT operation is achieved through variable frequency control. The input inductor of the proposed converter operates in CCM while maintaining the minimum current ripple from the input source, removing the need for an electrolytic capacitor at the input. Simulation and experimental results on a proof-of-concept hardware prototype have been provided to highlight the features and performance of the proposed converter.

REFERENCES

[1] "The first decade: 2004–2014," REN. [Online]. Available: http//www.ren21.net, Accessed on: Dec. 8, 2019.

[2] "2018 highlights," REN. [Online]. Available: http://www.ren21.net, Accessed on: Dec. 8, 2019.

[3] L. Huber and M. M. Jovanovic, "A design approach for server power supplies for networking," in *Proc. IEEE Appl. Power Electron. Conf. Expo.*, 2000, pp. 1163–1169.

[4] M. Adly and K. Strunz, "Irradiance-adaptive PV module integrated converter for high efficiency and power quality in standalone and DC microgrid applications," *IEEE Trans. Ind. Electron.*, vol. 65, no. 1, pp. 436–446, Jan. 2018.

[5] C. Pan, M. Cheng, C. Lai, and P. Chen, "Current-ripple-free module integrated converter with more precise maximum power tracking control for PV energy harvesting," *IEEE Trans. Ind. Appl.*, vol. 51, no. 1, pp. 271–278, Jan./Feb. 2015.

[6] M. Zhang, Y. Xing, H. Wu, H. Hu, and X. Ma, "A dual coupled inductors-based high step-up/step-down bidirectional dc-dc converter for energy storage system," in *Proc. IEEE Appl. Power Electron. Conf. Expo.*, 2017, pp. 2958–2963.

[7] W. Li, Y. Zhao, Y. Deng, and X. He, "Interleaved converter with voltage multiplier cell for high step-up and high-efficiency conversion," *IEEE Trans. Power Electron.*, vol. 25, no. 9, pp. 2397–2408, Sep. 2010.

[8] L. Yang, T. Liang, and J. Chen, "Transformerless DC–DC converters with high step-up voltage gain," *IEEE Trans. Ind. Electron.*, vol. 56, no. 8, pp. 3144–3152, Aug. 2009.

[9] S. H. Hosseini and T. Nouri, "A transformerless step-up dc-dc converter with high voltage gain and reduced voltage stresses on semiconductors," in *Proc. 47th Int. Univ. Power Eng. Conf.*, 2012, pp. 1–6.

[10] V. Samavatian and A. Radan, "A high efficiency input/output magnetically coupled interleaved buck–boost converter with low internal oscillation for fuel-cell applications: CCM steady-state Analysis," *IEEE Trans. Ind. Electron.*, vol. 62, no. 9, pp. 5560–5568, Sep. 2015.

[11] R. N. A. L. E Silva Aquino, F. L. Tofoli, P. P. Praca, D. D. S. Oliveira, and L. H. S. C. Barreto, "Soft switching high-voltage gain dc–dc interleaved boost converter," *IET Power Electron.*, vol. 8, no. 1, pp. 120–129, 2015.

[12] G. Yao, A. Chen, and X. He, "Soft switching circuit for interleaved boost converters," *IEEE Trans. Power Electron.*, vol. 22, no. 1, pp. 80–86, Jan. 2007.

[13] R. Moradpour, H. Ardi, and A. Tavakoli, "Design and implementation of a new SEPIC-based high step-up DC/DC converter for renewable energy applications," *IEEE Trans. Ind. Electron.*, vol. 65, no. 2, pp. 1290–1297, 2018.

[14] D. Fu and Y. Tang, "High step-up ZVS dual switches converter with three-winding-coupled inductor," in *Proc. IEEE Energy Convers. Congr. Expo.*, 2015, pp. 119–124.

[15] Y. Chen, Z. Li, and R. Liang, "A novel soft-switching interleaved coupled-inductor boost converter with only single auxiliary circuit," *IEEE Trans. Power Electron.*, vol. 33, no. 3, pp. 2267–2281, Mar. 2018.

[16] W. Li, Y. Zhao, X. He, D. Xu, and B. Wu, "Interleaved ZVS flyback-forward converter with reduced output voltage stress on secondary rectifier diodes," in *Proc. 26th Annu. IEEE Appl. Power Electron. Conf. Expo.*, 2011, pp. 1915–1919.

[17] M. R. Amini and H. Farzanehfard, "Novel family of PWM soft-single-switched DC–DC converters with coupled inductors," *IEEE Trans. Ind. Electron.*, vol. 56, no. 6, pp. 2108–2114, Jun. 2009.

[18] D. Jung, Y. Ji, S. Park, Y. Jung, and C. Won, "Interleaved soft-switching boost converter for photovoltaic power-generation system," *IEEE Trans. Power Electron.*, vol. 26, no. 4, pp. 1137–1145, Apr. 2011.

[19] A. B. Shitole, S. Sathyan, H. M. Suryawanshi, G. G. Talapur, and P. Chaturvedi, "Soft-switched high voltage gain boost-integrated flyback converter interfaced single-phase grid-tied inverter for SPV integration," *IEEE Trans. Ind. Appl.*, vol. 54, no. 1, pp. 482–493, Jan./Feb. 2018.

[20] H. Ardi, A. Ajami, and M. Sabahi, "A novel high step-up DC–DC converter with continuous input current integrating coupled inductor for renewable energy applications," *IEEE Trans. Ind. Electron.*, vol. 65, no. 2, pp. 1306–1315, Feb. 2018.

[21] R. Gules, W. M. Dos Santos, F. A. Dos Reis, E. F. R. Romaneli, and A. A. Badin, "A modified SEPIC converter with high static gain for renewable applications," *IEEE Trans. Power Electron.*, vol. 29, no. 11, pp. 5860–5871, Nov. 2014.

[22] H.-W. Seong, H.-S. Kim, K.-B. Park, G.-W. Moon, and M.-J. Youn, "High step-up DC-DC converters using zero-voltage switching boost integration technique and light-load frequency modulation control," *IEEE Trans. Power Electron.*, vol. 27, no. 3, pp. 1383–1400, Mar. 2012.

[23] M. Das and V. Agarwal, "Novel high-performance stand-alone solar PV system with high-gain high-efficiency DC–DC converter power stages," *IEEE Trans. Ind. Appl.*, vol. 51, no. 6, pp. 4718–4728, Nov./Dec. 2015.

[24] L. He, Z. Zheng, and D. Guo, "High step-up DC–DC converter with active soft-switching and voltage-clamping for renewable energy systems," *IEEE Trans. Power Electron.*, vol. 33, no. 11, pp. 9496–9505, Nov. 2018.

[25] S. Hasanpour, A. Baghramian, and H. Mojallali, "A modified SEPIC-based high step-up DC–DC converter with quasi-resonant operation for renewable energy applications," *IEEE Trans. Ind. Electron.*, vol. 66, no. 5, pp. 3539–3549, May 2019.

[26] L. Ferreira Costa and M. Liserre, "Failure analysis of the dc-dc converter: A comprehensive survey of faults and solutions for improving reliability," *IEEE Power Electron. Mag.*, vol. 5, no. 4, pp. 42–51, Dec. 2018.

[27] J. Falck, C. Felgemacher, A. Rojko, M. Liserre, and P. Zacharias, "Reliability of power electronic systems: An industry perspective," *IEEE Ind. Electron. Mag.*, vol. 12, no. 2, pp. 24–35, Jun. 2018.

[28] K. Kanathipan, S. Moury, and J. Lam, "A fast and accurate maximum power point tracker for a multi-input converter with wide range of soft-switching operation for solar energy systems," in *Proc. IEEE Appl. Power Electron. Conf. Expo.*, 2017, pp. 2076–2083.

Kajanan Kanathipan (Student Member, IEEE) received the master's degree in electrical and computer engineering from York University, Toronto, ON, Canada, in 2019. He is currently working toward the Ph.D. degree in electrical engineering with the Advanced Power Electronics Laboratory for Sustainable Energy Research, York University.

His research interests include design and control of power electronic converters for renewable energy applications.

Dr. Kanathipan was the recipient of the 2019 Ontario Graduate Scholarship.

Reza Emamalipour (Student Member, IEEE) received the B.S. degree in power engineering from Shahid Beheshti University, Tehran, Iran, in 2012, and the M.S. degree in power and energy systems from the Department of Electrical and Computer Engineering, University of Tehran, Tehran, Iran, in 2015. He is currently working toward the Ph.D. degree in power electronics with the Advanced Power Electronics Laboratory for Sustainable Energy Research, York University, Toronto, ON, Canada.

From 2011 to 2017, he was a Research Associate with the Energy and Automotive Technology Laboratory, University of Tehran, Tehran, Iran. His research interests include design and control of power electronics converters for renewable energy and energy storage systems, soft-switching bidirectional converters, speed control of electrical machines, and battery management systems.

John Lam (Senior Member, IEEE) received the master's and Ph.D. degrees in electrical engineering from Queen's University, Kingston, ON, Canada, in 2006 and 2010, respectively.

He is currently an Associate Professor with the Department of Electrical Engineering and Computer Science, York University, Toronto, ON, Canada. His research interests include power electronic converters with soft-switching techniques, wide bandgap-based power conversion systems, and renewable energy application.

Dr. Lam was the recipient of the 2018 Outstanding Reviewer Award in the IEEE TRANSACTIONS ON POWER ELECTRONICS. He is an Associate Editor of the IEEE TRANSACTIONS ON POWER ELECTRONICS.